Hydrostatic correction for sigma coordinate ocean models

Peter C. Chu and Chenwu Fan

Naval Ocean Analysis and Prediction Laboratory, Department of Oceanography, Naval Postgraduate School, Monterey, California, USA

Received 30 September 2002; revised 17 March 2003; accepted 4 April 2003; published 27 June 2003.

[1] How to reduce the horizontal pressure gradient error is a key issue in terrain-following coastal models. The horizontal pressure gradient splits into two parts, and incomplete cancellation of the truncation errors of those parts cause the error. Use of the finite volume discretization leads to a conserved scheme for pressure gradient computation that has better truncation properties with high accuracy. The analytical coastal topography and seamount test cases are used to evaluate the new scheme. The accuracy of the new scheme is comparable to the sixth-order combined compact scheme (with an error reduction by a factor of 70 comparing to the second-order scheme) with mild topography and much better than the sixth-order combined compact scheme with steep topography. The computational efficiency of the new scheme is comparable to the second-order difference scheme. The two characteristics, high accuracy and computational efficiency, make this scheme useful for the sigma coordinate ocean models. *INDEX TERMS:* 4255 Oceanography: General: Numerical modeling; 4263 Oceanography: General: Ocean prediction; 4243 Oceanography: General: Marginal and semienclosed seas; 4219 Oceanography: General: Continental shelf processes; 3337 Meteorology and Atmospheric Dynamics: Numerical modeling and data assimilation; *KEYWORDS:* sigma coordinate ocean model, horizontal pressure gradient error, hydrostatic correction, finite volume scheme, high-order scheme

Citation: Chu, P. C., and C. Fan, Hydrostatic correction for sigma coordinate ocean models, *J. Geophys. Res.*, *108*(C6), 3206, doi:10.1029/2002JC001668, 2003.

1. Introduction

[2] In regional oceanic (or atmospheric) prediction models, the effects of bottom topography must be taken into account and usually the terrain-following sigma coordinates should be used to imply the continuous topography. In sigma coordinates the water column is divided into the same number of grid cells regardless of the depth. Consider 2D problems for mathematical simplification. Let (x, z) be the Cartesian coordinates and $(\hat{x}, \sigma)$ be the sigma coordinates. The conventional relationships between z and sigma coordinates are given by

$$\hat{x} = x, \ \sigma = \frac{z - \eta}{H + \eta}, \tag{1}$$

where η is the surface elevation. Both z and σ increase vertically upward such that $z = \eta$, $\sigma = 0$ at the surface and $\sigma = -1$, $z = -H$ at the bottom. The horizontal pressure gradient becomes difference between two large terms

$$\frac{\partial p}{\partial x} = \frac{\partial \hat{p}}{\partial \hat{x}} - \frac{1}{H + \sigma}\left(\sigma \frac{\partial H}{\partial \hat{x}} + \frac{\partial \eta}{\partial x}\right)\frac{\partial \hat{p}}{\partial \sigma}, \tag{2}$$

that may cause large truncation error at steep topography [e.g., *Gary*, 1973; *Haney*, 1991; *Mellor et al.*, 1994; *McCalpin*, 1994; *Chu and Fan*, 1997, 1998, 1999, 2000, 2001; *Song*, 1998].

[3] Several methods have been suggested to reduce the truncation errors to acceptable levels: (1) smoothing topography [*Chu and Fan*, 2001], (2) subtracting a mean vertical density profile before calculating the gradient [*Gary*, 1973; *Mellor et al.*, 1994], (3) bringing certain symmetries of the continuous forms into the discrete level to ensure cancellations of these terms such as the density Jacobian scheme [e.g., *Mellor et al.*, 1998; *Song*, 1998; *Song and Wright*, 1998], (4) increasing numerical accuracy [e.g., *McCalpin*, 1994; *Chu and Fan*, 1997, 1998, 1999, 2000, 2001], (5) changing the grid from a sigma grid to a z level grid before calculating the horizontal pressure gradient [e.g., *Stelling and van Kester*, 1994]. *Kliem and Pietrzak* [1999] claimed that the z level based pressure gradient calculation is the most simple and effective means to reduce the pressure gradient errors. After comparing to other schemes, *Ezer et al.* [2002] show the favorable performance of the latest polynomial schemes. Recently, *Shchepetkin and McWilliams* [2002] design a pressure gradient algorithm with splines that achieves more accurate hydrostatic balance between the two components and that does not lose as much accuracy with nonuniform vertical grids at relatively coarse resolution.

[4] Using the finite volume integration approach [*Lin*, 1997], an extra hydrostatic correction term is added to the ordinary second-order scheme for reducing the horizontal pressure gradient error. With the extra term the discretiza-

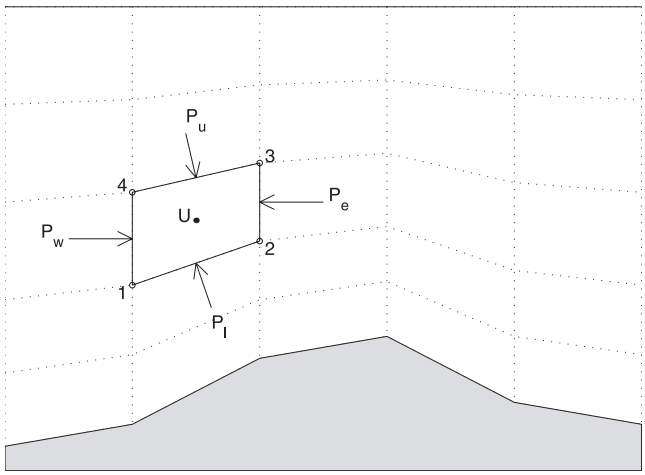

Figure 1. Finite volume discretization with staggered grid in a terrain-following coordinate system.

tion scheme is called the hydrostatic correction (HC) scheme. In this study, we describe the physical and mathematical bases of the HC scheme and its verification. The outline of this paper is as follows: Description of the horizontal gradient in finite volume is given in section 2. The second-order scheme is given in section 3. Hermit polynomial integration and hydrostatic correction are depicted in sections 4 and 5. Error estimation and seamount test case are given in sections 6 and 7. In section 8, the conclusions are presented.

2. Horizontal Pressure Gradient in Finite Volume

[5] Let the flow field change in *x*-*z* plane only (Figure 1). A finite volume (trapezoidal cylinder) is considered with the length of L_y (in the y direction) and the cross section represented by the shaded region (trapezoid) in Figure 1. The resultant pressure force (**F**) acting on the finite volume is computed as follows:

$$\mathbf{F} = L_y \oint_C p\mathbf{n}ds \tag{3}$$

where p is the pressure, C represents the four boundaries; **n** denotes the normal unit vector pointing inward; and ds is an element of the boundary. The contour integral is taken counterclockwise along the peripheral of the volume element. The pressure force exerts on the four boundaries of the finite volume with p_w, p_e, p_u, and p_l on the west, east, upper, and lower sides. The horizontal ($F_\mathbf{x}$) and vertical ($F_\mathbf{z}$) components of the resultant pressure force are computed by

$$F_x = -L_y\left(\int_1^2 p_l dz + \int_2^3 p_e dz + \int_3^4 p_u dz + \int_4^1 p_w dz\right), \tag{4}$$

$$F_z = L_y\left(\int_1^2 p_l dx + \int_3^4 p_u dx\right), \tag{5}$$

where points 1, 2, 3, and 4 are the four vertices of the finite volume. The hydrostatic balance is given by

$$F_z = g\Delta m, \tag{6}$$

where g is the gravitational acceleration, Δm is the mass of the finite volume. Equation (6) states that the vertical component of the resultant pressure force acting on the finite volume exactly balances the total weight of the finite volume.

[6] For a Boussinesq, hydrostatic ocean model, the pressure field is calculated by

$$p = p_{atm} + \rho_0 g\eta + g\int_z^0 \rho(x, z', t)dz', \tag{7}$$

where p_{atm} is the atmospheric pressure at the ocean surface, ρ_0 is the characteristic density, and η is the surface elevation. Substitution of (7) into (5) leads to

$$\begin{aligned} F_z &= gL_y\left(\int_1^2\int_z^0 \rho(x, z', t)dz'dx + \int_3^4\int_z^0 \rho(x, z', t)dz'dx\right) \\ &= gL_y\int_{\Delta S}\int \rho(x, z', t)dz'dx = g\Delta m, \end{aligned} \tag{8}$$

where ΔS is the area of the trapezoid (Figure 1) computed by

$$\Delta S = (x_{i+1} - x_i)\left(z_{i,k} + z_{i+1,k} - z_{i,k+1} - z_{i+1,k+1}\right), z_{i,k} = H_i \cdot \sigma_k. \tag{9}$$

Equation (8) indicates that the finite volume discretization guarantees the hydrostatic balance in Boussinesq, hydrostatic ocean models. Using equation (4) the horizontal pressure gradient is computed by

$$\frac{\partial p}{\partial x} \equiv \frac{F_x}{L_y\Delta S} = -\frac{1}{\Delta S}\left(\int_1^2 p_l dz + \int_2^3 p_e dz + \int_3^4 p_u dz + \int_4^1 p_w dz\right), \tag{10}$$

which has the flux form (i.e., the conserved scheme). In the conserved scheme, the pressure gradient for any grid cell is computed from the summation of pressure exerted on the four sides of the cell. For the whole domain integration, the pressure at any grid cell side not at the domain boundary is used twice with opposite sign (canceling each other). Thus equation (10) is called the conservation scheme. Finite difference schemes in the sigma coordinate such as second-order central difference scheme popularly used in ocean models as well as the recently developed spline-based scheme [*Shchepetkin and McWilliams*, 2002]. Since design of conservation scheme is a key issue in numerical modeling, the discretization (equation (10)) may improve the pressure gradient computation in terrain-following ocean models.

3. Second-Order Scheme

[7] In ocean models with the staggered grid (Figure 1), velocity is evaluated at the center of the volume and

pressure is put at the four vertices. With given values at vertices, we have several methods to compute four integrations in the right-hand side of (equation (10)). The mean value theorem leads to,

$$\int_1^2 p_l dz = \bar{p}_l\left(z_{i+1,k+1} - z_{i,k+1}\right), \int_2^3 p_e dz = \bar{p}_e\left(z_{i+1,k} - z_{i+1,k+1}\right),$$
$$\int_3^4 p_l dz = \bar{p}_u\left(z_{i,k} - z_{i+1,k}\right), \int_4^1 p_w dz = \bar{p}_w\left(z_{i,k+1} - z_{i,k}\right), \quad (11)$$

where $\bar{p}_l, \bar{p}_e, \bar{p}_u, \bar{p}_w$ are the mean values of pressure at the four sides of the trapezoid. The horizontal pressure gradient with the finite volume consideration is given by

$$\frac{\Delta p}{\Delta x} = \frac{1}{\Delta S}\left[\bar{p}_l\left(z_{i+1,k+1} - z_{i,k+1}\right) + \bar{p}_e\left(z_{i+1,k} - z_{i+1,k+1}\right) + \bar{p}_u\left(z_{i,k} - z_{i+1,k}\right) + \bar{p}_w\left(z_{i,k+1} - z_{i,k}\right)\right], \quad (12)$$

For the second-order staggered grid, $\bar{p}_l, \bar{p}_e, \bar{p}_u, \bar{p}_w$, are taken as the arithmetic means of pressure at the two vertices,

$$\bar{p}_w \simeq \frac{p_{i,k} + p_{i,k+1}}{2}, \quad \bar{p}_e \simeq \frac{p_{i+1,k} + p_{i+1,k+1}}{2},$$
$$\bar{p}_l \simeq \frac{p_{i,k+1} + p_{i+1,k+1}}{2} \quad \bar{p}_u \simeq \frac{p_{i,k} + p_{i+1,k}}{2}. \quad (13)$$

Substitution of equation (13) into equation (12) and Use of equation (1) lead to

$$\left(\frac{\Delta p}{\Delta x}\right)_{i,k} = \frac{\left(p_{i+1,k+1} - p_{i,k}\right)\left(H_{i+1}\sigma_k - H_i\sigma_{k+1}\right) + \left(p_{i+1,k} - p_{i,k+1}\right)\left(H_i\sigma_k - H_{i+1}\sigma_{k+1}\right)}{\Delta x_i \Delta\sigma_k\left(H_i + H_{i+1}\right)}, \quad (14)$$

where $\Delta x_i = x_{i+1} - x_i$ and $\Delta\sigma_k = \sigma_k - \sigma_{k+1}$. Equation (14) is the discretization of the horizontal pressure gradient with the finite volume consideration.

[8] Finite difference schemes are commonly used in sigma coordinate ocean models. For the sigma coordinate system,

$$z_{i,k} = H_i \cdot \sigma_k, \quad (15)$$

the horizontal pressure gradient (2) discretized by the central difference scheme is

$$\left(\frac{\Delta p}{\Delta x}\right)_{i,k} = \frac{p_{i+1,k} + p_{i+1,k+1} - p_{i,k} - p_{i,k+1}}{2\Delta x_i} - \left(\frac{\sigma_k + \sigma_{k+1}}{H_i + H_{i+1}}\right) \cdot \left(\frac{H_{i+1} - H_i}{\Delta x_i}\right)\left(\frac{p_{i,k} + p_{i+1,k} - p_{i,k+1} - p_{i+1,k+1}}{2\Delta\sigma_k}\right)$$
$$= \frac{\left(p_{i+1,k+1} - p_{i,k}\right)\left(H_{i+1}\sigma_k - H_i\sigma_{k+1}\right) + \left(p_{i+1,k} - p_{i,k+1}\right)\left(H_i\sigma_k - H_{i+1}\sigma_{k+1}\right)}{\Delta x_i \Delta\sigma_k\left(H_i + H_{i+1}\right)},$$

which is exactly the same as equation (14). Thus the second-order finite volume scheme is the same as the finite difference scheme for the staggered grid.

[9] Discretization of pressure integration along the segments (equation (11)) has two weaknesses: (1) low accuracy (second-order) and (2) pure mathematical, which means the physical property of p is not considered. Since most sigma coordinate ocean models are hydrostatically balanced,

$$\frac{\partial p}{\partial z} = -\rho g, \quad (16)$$

one way to increase accuracy is to use Hermit Polynomial.

4. Hermit Polynomial Integration

[10] Suppose p and its directional derivative $\partial p/\partial l$ be given at two vertices of a segment of $[l_1, l_2]$ of any finite volume in Figure 1. Let

$$\xi = \frac{l - l_1}{\Delta l}, \quad \Delta l \equiv l_2 - l_1. \quad (17)$$

ξ varies in [0, 1]. The integration of p along the segment from l_1 to l_2 is given by,

$$\int_{l_1}^{l_2} p(l) dl = \Delta l \int_0^1 \Psi(\xi) d\xi, \quad (18)$$

where

$$\Psi(\xi) = p_{l_1}\Phi_1 + p_{l_2}\Phi_2 + \Delta l\left(\frac{\partial p}{\partial l}\right)_{l_1}\Phi_3 + \Delta l\left(\frac{\partial p}{\partial l}\right)_{l_2}\Phi_4, \quad (19)$$

is the Hermit polynomial and

$$\Phi_1 = 1 - 3\xi^2 + 2\xi^3, \quad \Phi_2 = 3\xi^2 - 2\xi^3,$$
$$\Phi_3 = \xi - 2\xi^2 + \xi^3, \quad \Phi_4 = \xi^3 - \xi^2, \quad (20)$$

are the four basis functions. Substitution of equations (19) and (20) into (18) leads to

$$\int_{l_1}^{l_2} p dl = \int_0^1 \Psi(\xi) d\xi = \frac{\Delta l}{2}(p_1 + p_2) + \frac{\Delta l^2}{12}\left(\left(\frac{\partial p}{\partial l}\right)_1 - \left(\frac{\partial p}{\partial l}\right)_2\right). \quad (21)$$

5. Hydrostatic Correction

[11] From the hydrostatic balance (equation (16)), the pressure integration along the two vertical segments of a finite volume is calculated analytically by (taking east side in Figure 1 as an example)

$$\int_2^3 p_e dz = \frac{(z_3 - z_2)}{2}(p_2 + p_3) - \frac{(z_3 - z_2)^2 g}{12}(\rho_2 - \rho_3). \quad (22)$$

For upper and lower segments of the finite volume (Figure 1), directional derivative needs to be computed

$$\frac{\partial p}{\partial l} = \cos\alpha\frac{\partial p}{\partial x} + \sin\alpha\frac{\partial p}{\partial z} = \cos\alpha\frac{\partial p}{\partial x} - \rho g \sin\alpha, \quad (23)$$

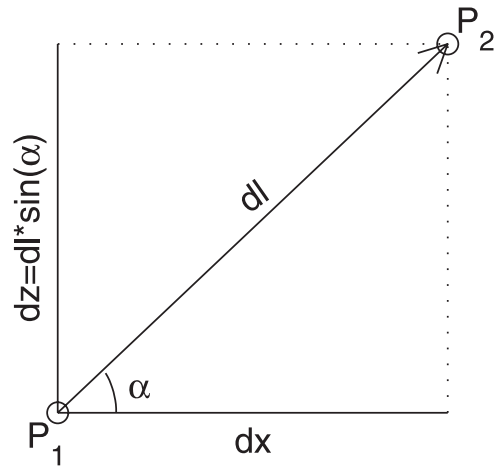

Figure 2. Directional derivative of pressure along upper or lower segment.

where α is the angle between the segment and the *x axis* (Figure 2). The pressure integration along the upper and lower segments is calculated by (lower segment as an example)

$$\int_1^2 p_l dz = \sin\alpha \int_{l_1}^{l_2} p dl \simeq \frac{(z_2 - z_1)}{2}(p_1 + p_2) - \frac{(z_2 - z_1)^2 g}{12} \cdot(\rho_1 - \rho_2) + \frac{1}{12}\left(\frac{\partial p}{\partial x}|_1 - \frac{\partial p}{\partial x}|_2\right)(x_1 - x_2)(z_1 - z_2). \tag{24}$$

Thus integration along the four segments of the finite volume (Figure 1) is represented by

$$\int_m^n p dz \simeq \frac{(z_n - z_m)}{2}(p_m + p_n) - \frac{(z_n - z_m)^2 g}{12}(\rho_m - \rho_n) + \frac{1}{12}\left(\frac{\partial p}{\partial x}|_m - \frac{\partial p}{\partial x}|_n\right)(x_m - x_n)(z_m - z_n). \tag{25}$$

In the right-hand side, the first term is from the mean value calculation, and the second term is the hydrostatic correction. Substitution of equation (25) into equation (10) and neglect of high-order terms lead to

$$\left(\frac{\Delta p}{\Delta x}\right)_{i,k} \simeq \frac{\left[(p_{i+1,k+1} - p_{i,k})(z_{i+1,k} - z_{i,k+1}) + (p_{i+1,k} - p_{i,k+1})(z_{i,k} - z_{i+1,k+1})\right]}{(x_{i+1} - x_i)(z_{i,k} + z_{i+1,k} - z_{i,k+1} - z_{i+1,k+1})} + \Omega_{ik}, \tag{26}$$

where

$$\Omega_{ik} = \frac{g\Gamma_{ik}}{6(x_{i+1} - x_i)(z_{i,k} + z_{i+1,k} - z_{i,k+1} - z_{i+1,k+1})},$$

$$\Gamma_{ik} \equiv \Big[(H_{i+1}\sigma_k - H_{i+1}\sigma_{k+1})^2(\rho_{i+1,k} - \rho_{i+1,k+1}) - (H_i\sigma_k - H_i\sigma_{k+1})^2(\rho_{i,k} - \rho_{i,k+1}) + (H_{i+1}\sigma_{k+1} - H_i\sigma_{k+1})^2 \cdot (\rho_{i+1,k+1} - \rho_{i,k+1}) - (H_{i+1}\sigma_k - H_i\sigma_k)^2(\rho_{i+1,k} - \rho_{i,k})\Big]. \tag{27}$$

[12] The new correction term Ω_{ik} is in some sense equivalent to the common practice in Princeton Ocean Model (POM) [*Blumberg and Mellor*, 1987] of removing a vertical mean density profile [*Mellor et al.*, 1994], though here is done locally, while in the standard POM code the mean density profile is usually based on area averaged climatology and requires interpolation of the mean density profile to the sigma grid. In the sigma coordinate ocean models, equation (26) becomes

$$\left(\frac{\Delta p}{\Delta x}\right)_{i,k} \simeq \frac{\left[(p_{i+1,k+1} - p_{i,k})(H_{i+1}\sigma_k - H_i\sigma_{k+1}) + (p_{i+1,k} - p_{i,k+1})(H_i\sigma_k - H_{i+1}\sigma_{k+1})\right]}{\Delta x_i \Delta\sigma_k (H_i + H_{i+1})} + \Omega_{ik}. \tag{28}$$

The scheme (28) is evaluated with the coastal and seamount topography. The horizontal pressure gradient is computed using equations (27) and (28).

6. Error Estimation

6.1. Analytical Coastal Topography

[13] Choose coordinates such that the *y axis* coincides with the coast, and the *x*-axis points offshore. Cross-coastal topography consists of shelf, slope, and deep layer (Figure 3a). Analytical bottom topography is proposed in a way that shelf and slope are arcs of two circles. The shelf has a smaller radius (r), and the slope has a larger radius (R). The two arcs are connected such that the tangent of the bottom topography, dh/dx, is continuous at the shelf break ($x = x_0$). This requirement is met using the same maximum expanding angle (θ) for both arcs (Figure 3b). Thus θ represents the maximum slope angle. This bottom topography has three degrees of freedom: r, R, and θ. The maximum water depth is given by (Figure 3b)

$$H = (r + R)(1 - \cos\theta), \tag{29}$$

The horizontal, vertical coordinates, radii (r, R), and water depth are nondimensionalized by

$$x^* = \frac{x}{H}, \quad z^* = \frac{z}{H}, \quad r^* = \frac{r}{H}, \quad R^* = \frac{R}{H}, \quad h^* = \frac{h}{H}. \tag{30}$$

The analytical bottom topography representing shelf, slope, and deep layer (Figure 3) is given by

$$h^*(x^*) = \begin{cases} r^* - \sqrt{r^{*^2} - x^{*^2}}, & \text{if } (x^* \le x_0^*) \\ 1 - R^* + \sqrt{R^{*^2} - (x_1^* - x^*)^2}, & \text{if } (x_0^* < x^* \le x_1^*) \\ 1, & \text{if } (x^* > x_1^*) \end{cases} \tag{31}$$

Let the ratio between the two radii be defined by

$$k = \frac{r}{R}, \tag{32}$$

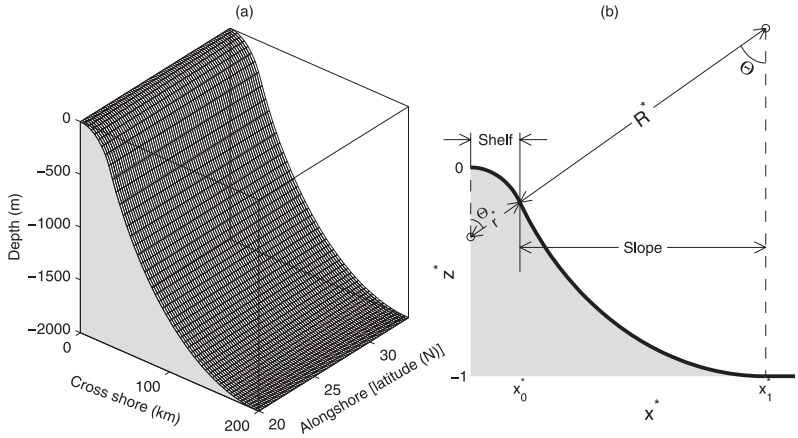

Figure 3. Coastal geometry with open boundaries: (a) three-dimensional view and (b) cross-coastal view.

Substitution of equations (29) and (32) into equation (30) leads to

$$r^* = \frac{k}{(1+k)(1-\cos\theta)}, \quad R^* = \frac{1}{(1+k)(1-\cos\theta)},$$
$$x_0^* = r^* \sin\theta = \frac{k \cdot \sin\theta}{(1+k)(1-\cos\theta)}, \tag{33}$$
$$x_1^* = (r^* + R^*)\sin\theta = \frac{\sin\theta}{1-\cos\theta}.$$

The shelf and slope widths are x_0^* and $(x_1^* - x_0^*)$, respectively. Use of equations (32) and (33) leads to

$$x_0^*/(x_1^* - x_0^*) = r^*/R^* = k \tag{34}$$

which indicates that the nondimensional parameter k is the ratio between shelf and slope widths. Thus the nondimensional bottom topography (equation (31)) has two degrees of freedom: k and θ. Figure 4 shows the coastal topography varying with the maximum slope angle θ (10°, 30°, 60°, 90°) and the shelf slope ratio k (0.1, 0.5, 1). The larger the angle θ, the steeper the bottom topography is; the lager the k, the shorter the slope is.

6.2. Nondimensional Pressure

[14] Let ρ_0 (1,025 kg m^{-3}) be the characteristic density. The density (ρ) and pressure (p) are nondimensionalized by

$$\rho^* = \frac{\rho}{\rho_0}, \quad p^* = \frac{p}{\rho_0 g H}, \tag{35}$$

and the hydrostatic balance (equation (16)) is nondimensionalized by

$$\frac{\partial p^*}{\partial z^*} = -\rho^*. \tag{36}$$

Integration of equation (36) from the ocean surface to depth z* leads to

$$p^* = \int_{z^*}^{0} \rho^* dz^* + p_a^*, \tag{37}$$

where p_a^* is the nondimensional atmospheric pressure. Since the horizontal atmospheric pressure gradient does not depend on the ocean bottom topography (or selection of the oceanic coordinate system), its effect on the sigma coordinate error (ocean) is neglected in this study.

6.3. Methodology

[15] Error reduction by the hydrostatic correction term (Ω_{ik}) is evaluated using the motionless ocean with an exponentially stratified density [*Chu and Fan*, 1997],

$$\rho^* = 1 + 0.005\left(1 - e^{2z^*}\right), \tag{38}$$

which leads to the fact that the pressure p^* depends only on z* (atmospheric pressure effect neglected) and no horizontal pressure gradient exists. However, computation in the sigma coordinate leads to false horizontal pressure gradient that is regarded as the sigma coordinate error.

[16] The horizontal pressure gradient $\delta p^*/\delta x^*$ is computed for x^* from 0 to 12 from the density field (equation (38)) with the analytical bottom topography (equation (31)) using

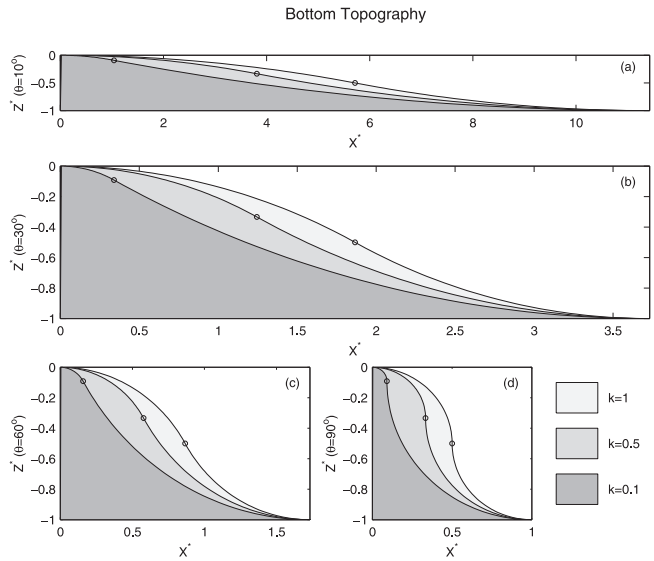

Figure 4. Dependence of bottom topography on k values for different values of maximum slope θ: (a) 10°, (b) 30°, (c) 60°, and (d) 90°.

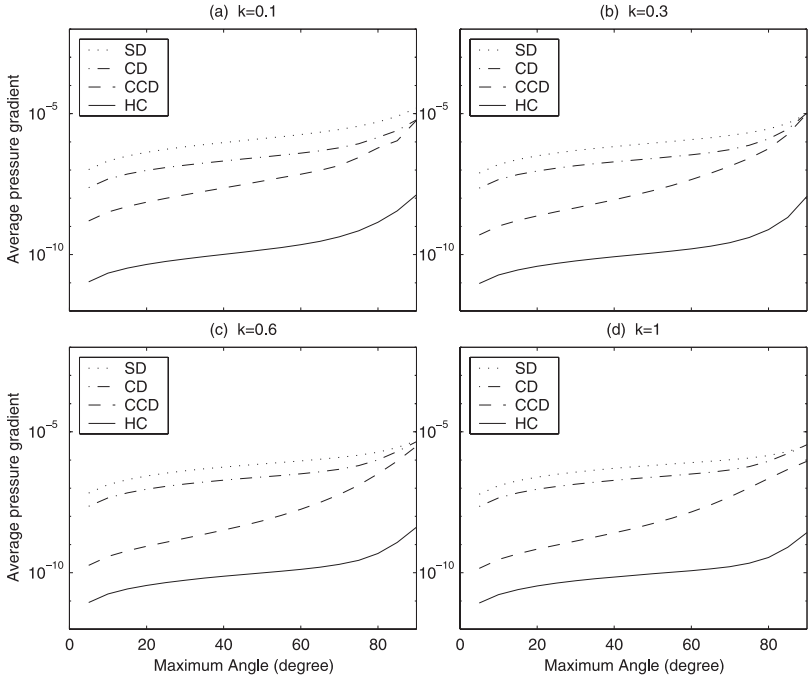

Figure 5. Dependence of GME on the maximum slope (θ value) for different k values: (a) 0.1, (b) 0.3, (c) 0.6, and (d) 1.0. Note that the four curves in each panel represent the SD (dotted), CD (dot-dashed), CCD (dashed), and HC (solid) schemes.

four different schemes: second-order difference (SD) scheme (equation (14)), fourth-order compact difference (CD) scheme [*Chu and Fan*, 1998], sixth-order combined compact difference (CCD) scheme [*Chu and Fan*, 1998], and the hydrostatic correction (HC) scheme (equation (28)). The accuracy of these schemes is evaluated by various mean and maximum values of the horizontal pressure gradient errors.

6.4. Global Performance

[17] The global performance of the four schemes is evaluated by the global mean (over all the grid points) of the

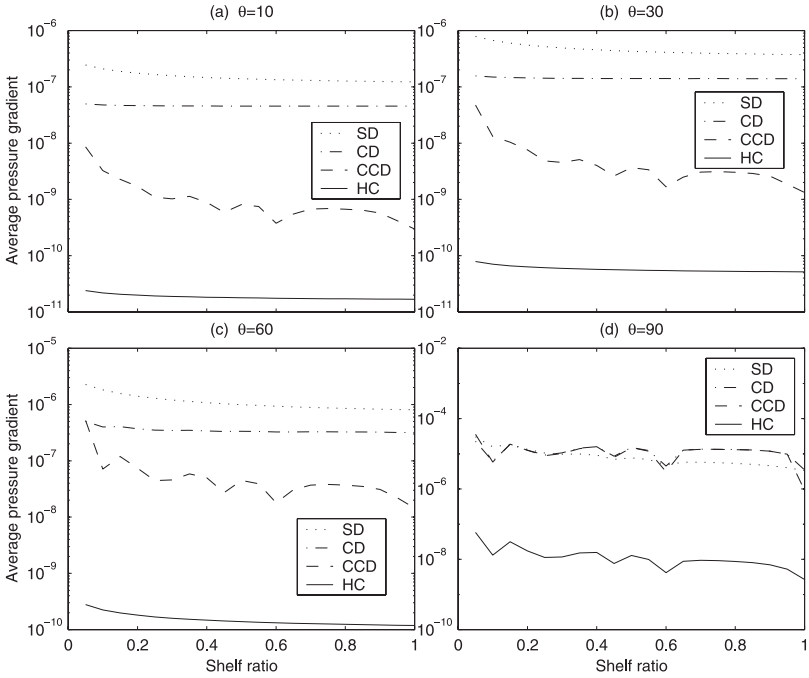

Figure 6. Dependence of GME on the shelf slope ratio (k value) for different θ value: (a) 10°, (b) 30°, (c) 60°, and (d) 90°. Note that the four curves in each panel represent the SD (dotted), CD (dot-dashed), CCD (dashed), and HC (solid) schemes.

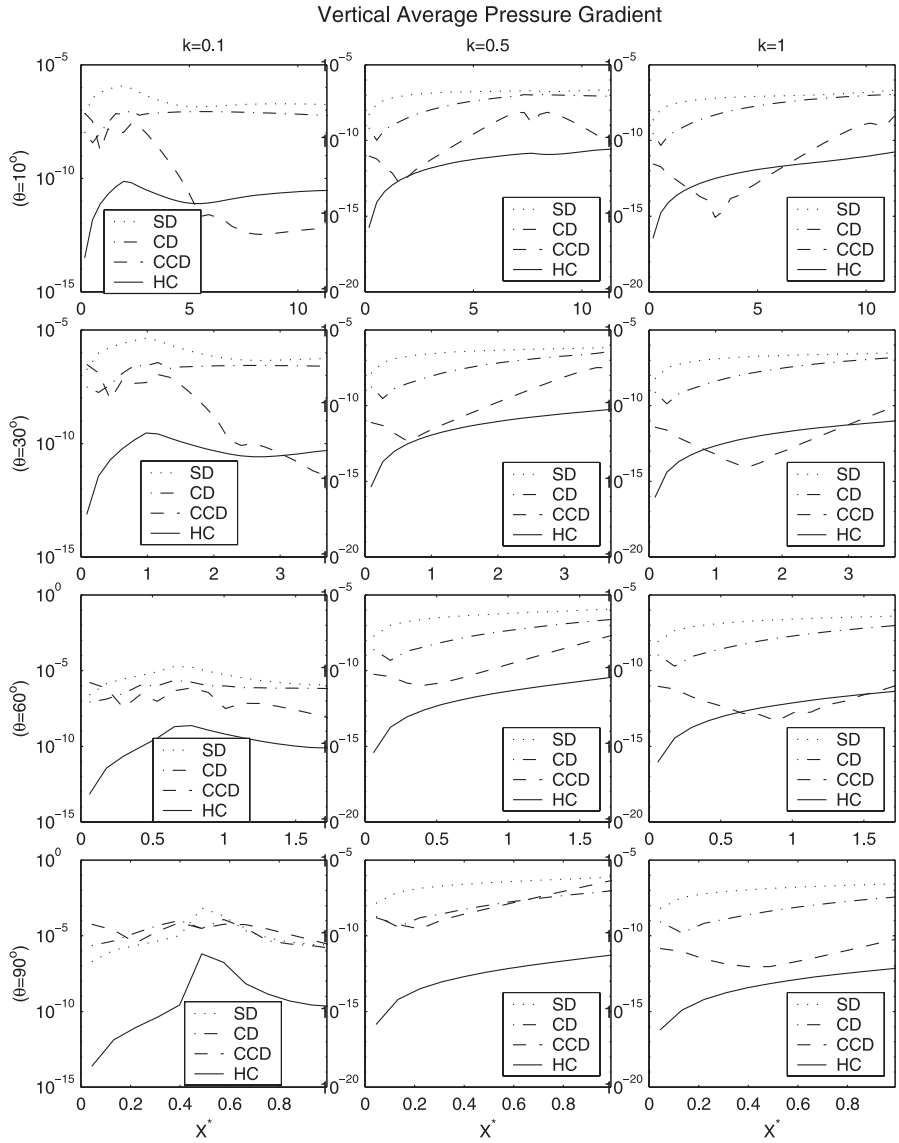

Figure 7. Dependence of VME on the offshore distance (x*) for three k values (0.1, 0.5, and 1) and four θ values (10°, 30°, 60°, and 90°). Note that each panel has four curves representing SD (dotted), CD (dot-dashed), CCD (dashed), and HC (solid) schemes.

absolute values of the horizontal pressure gradient, denoted by global mean error (GME). GME is computed using the four schemes for various k (0.1 to 1.0) and θ (5° to 90°). Figure 5 shows the dependence of GME on the maximum slope angle θ with four different values of the shelf/slope ratio: k = 0.1, 0.3, 0.6, 1. On each panel (a particular value of k), four curves are plotted representing the four schemes: SD, CD, CCD, and HC. For all the four schemes, GME increases with the maximum slope θ monotonically. However, GME reduces from SD to CD, from CD to CCD, and from CCD to HC schemes. Taking k = 0.1 and θ varies from 5° to 90°, GME increases from 1.04×10^{-7} to 1.58×10^{-5} using the SD scheme, from 2.37×10^{-8} to 6.08×10^{-6} using the CD scheme, from 1.58×10^{-9} to 5.82×10^{-6} for the CCD scheme; and from 1.09×10^{-11} to 1.31×10^{-8}. The overall error reduces drastically using the HC scheme.

[18] Figure 6 shows the dependence of GME on the shelf slope ratio (k) with four different maximum slopes: θ = 10°, 30°, 60°, and 90°. On each panel (a particular value of θ), four curves are plotted representing the four schemes: SD, CD, CCD, and HC. The same as Figure 5, GME greatly reduces using the HC scheme, compared to using the three currently used schemes (SD, CD, and CCD). For not very steep topography (Figures 6a–6c), GME reduces from SD to CD, from CD to CCD, and from CCD to HC schemes.

[19] For very steep topography (Figure 6d, θ = 90°), GME is comparable using any of the existing schemes (SD, CD, CCD), but 2–3 orders of magnitude smaller using the HC scheme. Such a high performance makes the HC scheme valuable for coastal modeling.

6.5. Cross-Coastal Error

[20] The cross-coastal error is evaluated by the vertical mean (over a water column) of the absolute values of the horizontal pressure gradient, denoted by vertical mean error (VME). VME is computed using the four schemes for three

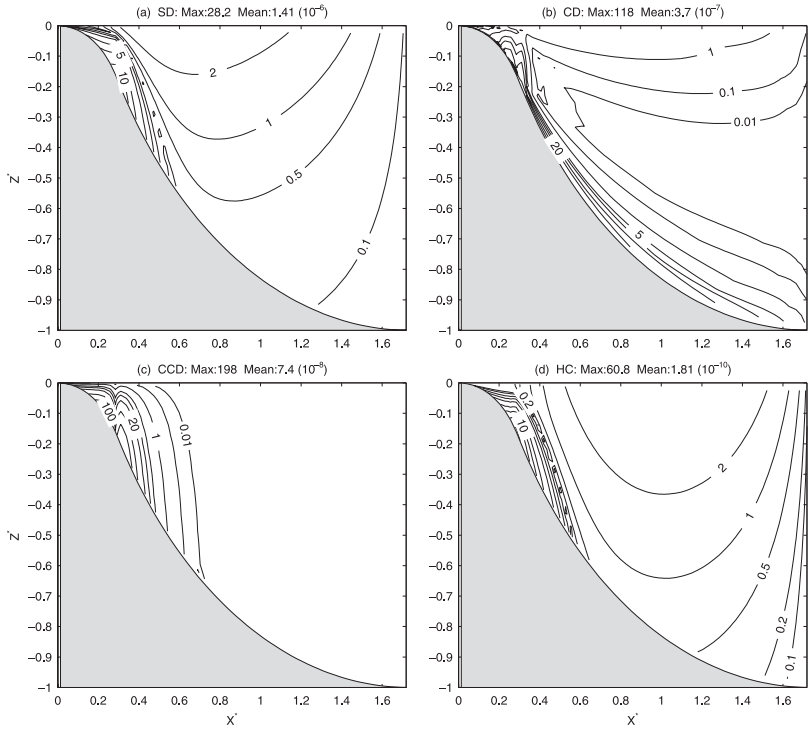

Figure 8. Contour of the absolute values of the horizontal pressure gradient (with $\theta = 60°$ and $k = 0.2$) calculated using: (a) SD, (b) CD, (c) CCD, and (d) HC schemes.

k values (0.1, 0.5, 1.0) and four θ values (10°, 30°, 60°, 90°). Each panel in Figure 7 shows the dependence of VME on the offshore distance (x^*) with four different schemes for a particular combination of the (k, θ) values. For the SD and HC schemes, VME usually has a minimum value at the coast ($x^* = 0$) and increases with x^* from shelf to slope. For the CD and CCD schemes, however, VME has a relatively large value at the coast, reduces with x^* to shelf break and then increases with x^* in the slope. This is caused by additional condition such as $\partial^2 p/\partial x^2 = 0$ is added at the coast ($x^* = 0$). The HC scheme reduces around 10^5 times of VME comparing to the SD scheme, around 10^4 times of VME comparing to the CD scheme, and around $10-10^3$ times of VME comparing to the CCD scheme.

[21] Figure 8 shows the contour of the absolute values of the pressure gradient (with $\theta = 60°$ and $k = 0.2$) calculated using the four schemes. Large errors occur near the bottom topography for all the schemes. However, the error reduces from SD to CD, from CD to CCD, and from CCD to HC schemes. The maximum error reduces by a factor of 2.39 from SD to CD scheme, a factor of 5.96 from CD to CCD scheme, and a factor of 32.57 from CCD to HC scheme. GME reduces by a factor of 3.81 from SD to CD scheme, a factor of 5.00 from CD to CCD scheme, and a factor of 408.8 from CCD to HC scheme (Table 1). High GME error reduction of the HC scheme is expected since the entire error in those tests is due to the vertical density gradient (see equation (38)). Removal of the hydrostatic term (or hydrostatic correction) removes most of the error.

Table 1. Comparison of Maximum and Global Mean Horizontal Pressure Gradient Errors Among Four Schemes Using the Analytical Coastal Bottom Topography With $\theta = 60°$ and $k = 0.2$

	Maximum Error	Global Mean Error
SD	28.2×10^{-6}	1.41×10^{-6}
CD	11.8×10^{-6}	0.37×10^{-6}
CCD	1.98×10^{-6}	0.74×10^{-7}
HC	6.08×10^{-9}	1.81×10^{-10}

7. Seamount Test Case

7.1. Known Solution

[22] Accuracy of any numerical scheme should be evaluated by either analytical or known solution. For a realistic ocean model, the analytical solution is hard to find. Consider

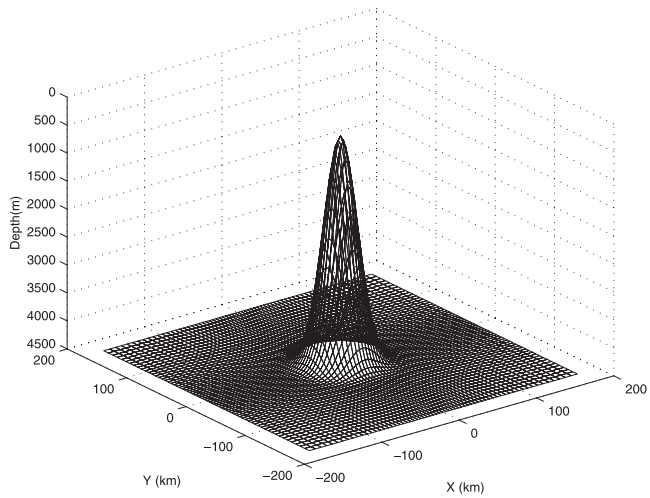

Figure 9. Seamount geometry.

a horizontally homogeneous and stably stratified ocean with realistic topography. Without forcing, initially motionless ocean will keep motionless forever, that is to say, we have a know solution ($\mathbf{V} = 0$). Any nonzero model velocity can be treated as an error. *Ezer et al.* [2002] evaluated seven different schemes and found that the sixth-order CCD scheme is accurate but computationally expensive. Thus we use the standard POM seamount test case to verify the performance of HC scheme, comparing with the SD and CCD schemes both in accuracy and computational efficiency.

7.2. Configuration

[23] A seamount is located in the center of a square channel with two solid, free slip boundaries in the north and south (Figure 9). The bottom topography is defined by [*Ezer et al.*, 2002]

$$H(x,y) = H_{\max}\left\{1 - A\exp\left[-\left(x^2+y^2\right)/L^2\right]\right\}, \qquad (39)$$

where $H_{\max}$ is the maximum depth (4,500 m); L is the seamount width; and $(1 - A)$ represents the depth of the seamount tip. In this study, we use a "very steep" case with $A = 0.9$ and $L = 25$ km.

[24] Unforced flow over the seamount in the presence of resting, level isopycnals is an idea test case for the assessment of pressure gradient errors in simulating stratified flow over topography. The flow is assumed to be reentrant (periodic) in the along the two open boundaries of the channel. We use this standard seamount case of POM to test the performance of the HC scheme. POM is the sigma coordinate model. In the horizontal directions the model uses the C grid and the second-order finite difference discretization except for the horizontal pressure gradient, which the user has choice of either second-order SD or sixth-order CCD schemes. There are 21 sigma levels. For each level, the horizontal model grid includes 64×64 grid cells with nonuniform size with finer resolution near the seamount,

$$\begin{aligned}\Delta x_i &= \Delta x_{\max} - \frac{1}{2}\Delta x_{\max}\sin\left(\frac{i\pi}{64}\right),\\ \Delta y_j &= \Delta y_{\max} - \frac{1}{2}\Delta y_{\max}\sin\left(\frac{j\pi}{64}\right),\end{aligned} \qquad (40)$$

where $\Delta x_{\max} = \Delta y_{\max} = 8$ km, denoting the grid size at the four boundaries. Temporal discretization is given by

$$(\Delta t)_{ex} = 6 \text{ s}, \ (\Delta t)_{in} = 30\ (\Delta t)_{ex}, \qquad (41)$$

where $(\Delta t)_{ex}$ and $(\Delta t)_{in}$ are external and internal time steps, respectively.

[25] POM is integrated from motionless state with an exponentially stratified temperature (°C) field

$$T(x,y,z) = 5 + 15\exp(z/H_T), \quad H_T = 1000 \text{ km}, \qquad (42)$$

and constant salinity (35 ppt) using three different schemes: SD, CCD and HC. During the integration, a constant density, 1000 kg m^{-3}, has been subtracted for the error reduction. The Laplacian Smargorinsky diffusion set up in the standard POM seamount test case is used in this study.

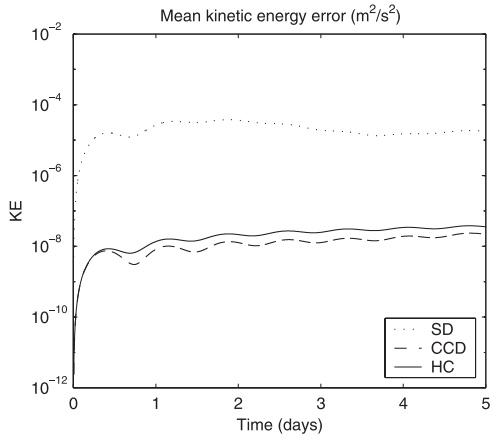

Figure 10. Temporally varying MKE (m^2 s^{-2}) using SD (dotted), CCD (dashed), and HC (solid) schemes.

[26] It is found that 5 days are sufficient for the model mean kinetic energy (MKE) per unit mass,

$$MKE = \frac{\iiint \frac{1}{2}\rho \mathbf{V}^2 dxdydz}{\iiint \rho dxdydz}$$

to reach quasi-steady state under the imposed conditions (Figure 10) for all the three schemes. Here, $\mathbf{V}$ is the error velocity. Thus we use the first 5 days of model output inside the region of (-169.35 km $\leq x \leq 169.35$ km, -169.35 km $\leq y \leq 169.35$ km) to compare the HC scheme to the SD and CCD schemes. Feasibility of using the HC scheme is twofold: (1) drastic error reduction and (2) no drastic CPU time increase. The following two quantities are used to compare the errors: the volume-integrated pressure gradient and the vertically integrated velocity.

7.3. Volume-Integrated Horizontal Pressure Gradient

[27] The volume-integrated horizontal pressure gradient ($\partial p/\partial x$) for a finite volume ($Hd\sigma dxdy$) with its center at (x, y, σ), denoted by VIPG, is used to represent the sigma coordinate errors. Figure 11 shows VIPG at day 5 for the second-order SD, sixth-order CCD, and HC schemes at four sigma levels: k_σ = 5, 10, 15, and 20 (k_σ = 0 at the surface, and k_σ = 21 at the bottom). VIPG reveals a dipole pattern at east and west of the seamount at the upper half water column (k_σ = 5, 10), and a quadruple dipole in the lower layer. VIPG increases with depth from the surface (maximum 3.41×10^4 N) to the bottom (maximum 3.98×10^5 N) using the SD scheme). It reduces greatly using both CCD and HC schemes. Taking $k_\sigma = 10$ as an example, the maximum VIPG is 2.01×10^5 N using the SD scheme, 3.42×10^3 N using the sixth-order CCD scheme, and 3.05×10^3 N using the HC scheme. This indicates that the HC scheme has a comparable accuracy as the sixth-order CCD scheme and reduces the errors by a factor of 70 comparing to the SD scheme.

7.4. Vertically Integrated Velocity

[28] Owing to a very large number of calculations performed, we discuss the results exclusively in terms of

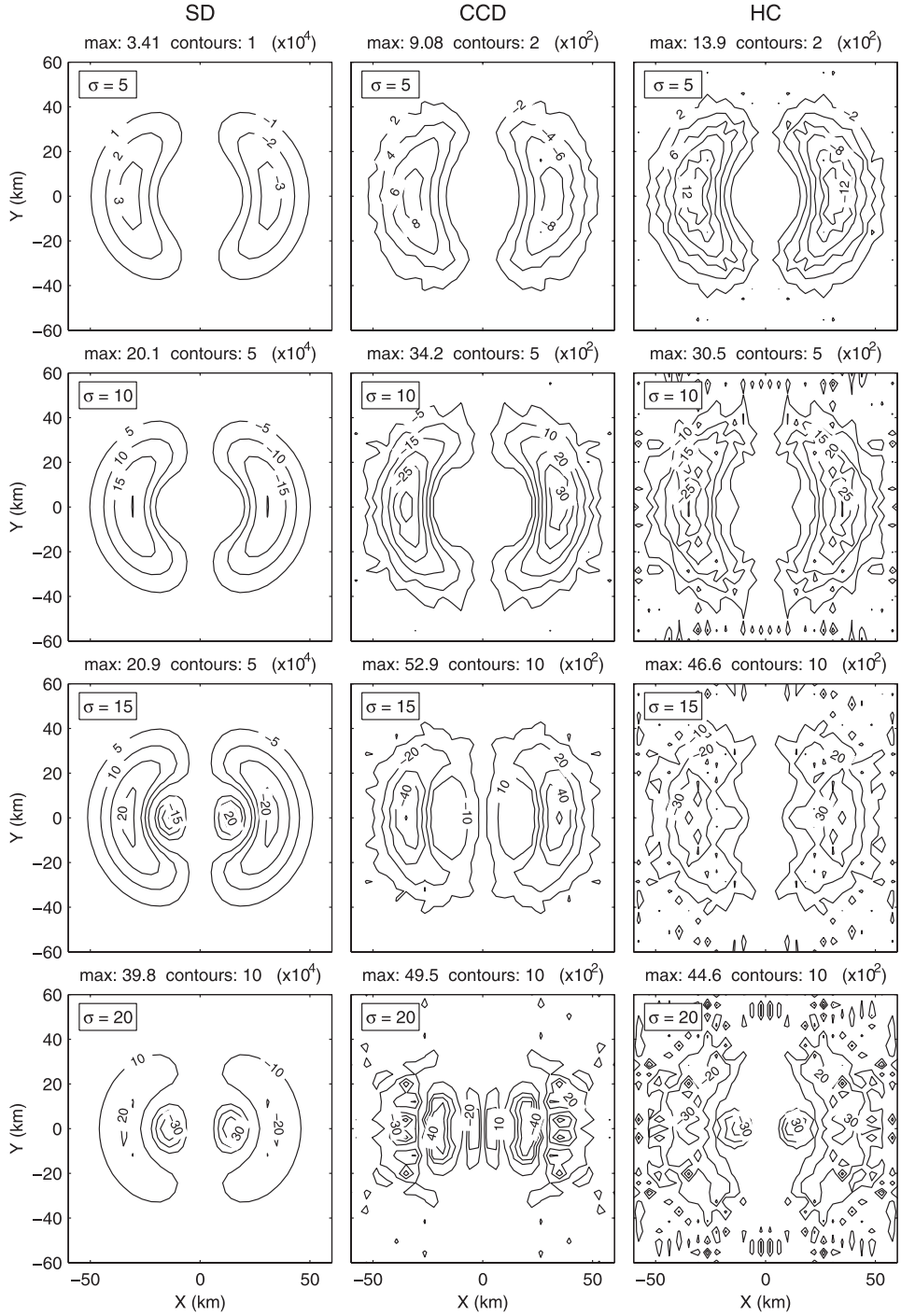

Figure 11. VIPG (unit: N) on day 5 at four sigma levels: k_σ = 5, 10, 15, and 20 (k_σ = 0 at the surface, and k_σ = 21 at the bottom) using SD, CCD, and HC schemes.

the vertically integrated velocity ($\mathbf{V}_{\text{int}}$) generated by the pressure gradient errors. Figure 12 shows the time evolution of the vertically integrated error velocity for day 1, day 2, day 4, and day 5 using the SD, CCD, and HC schemes.

[29] The vertically integrated velocity ($\mathbf{V}_{\text{int}}$) has a large-scale eight-lobe pattern centered on the seamount. This symmetric structure can be found in all the fields. However, its maximum values are around 0.05–0.1 $m^2\ s^{-1}$ using the SD scheme, 0.001–0.002 $m^2\ s^{-1}$ using the CCD and HC schemes. After 5 days of integration, the model generates spurious vertically integrated currents of O(0.09 $m^2\ s^{-1}$) using the SD scheme and of O(0.0015 $m^2\ s^{-1}$) using the CCD and HC schemes. Thus the HC scheme has the same accuracy as the sixth-order CCD scheme.

7.5. Computational Efficiency

[30] The numerical integration of POM using the three schemes was performed using SGI-Origin 200 machine. The CPU time was recorded at the end of day 5 integration.

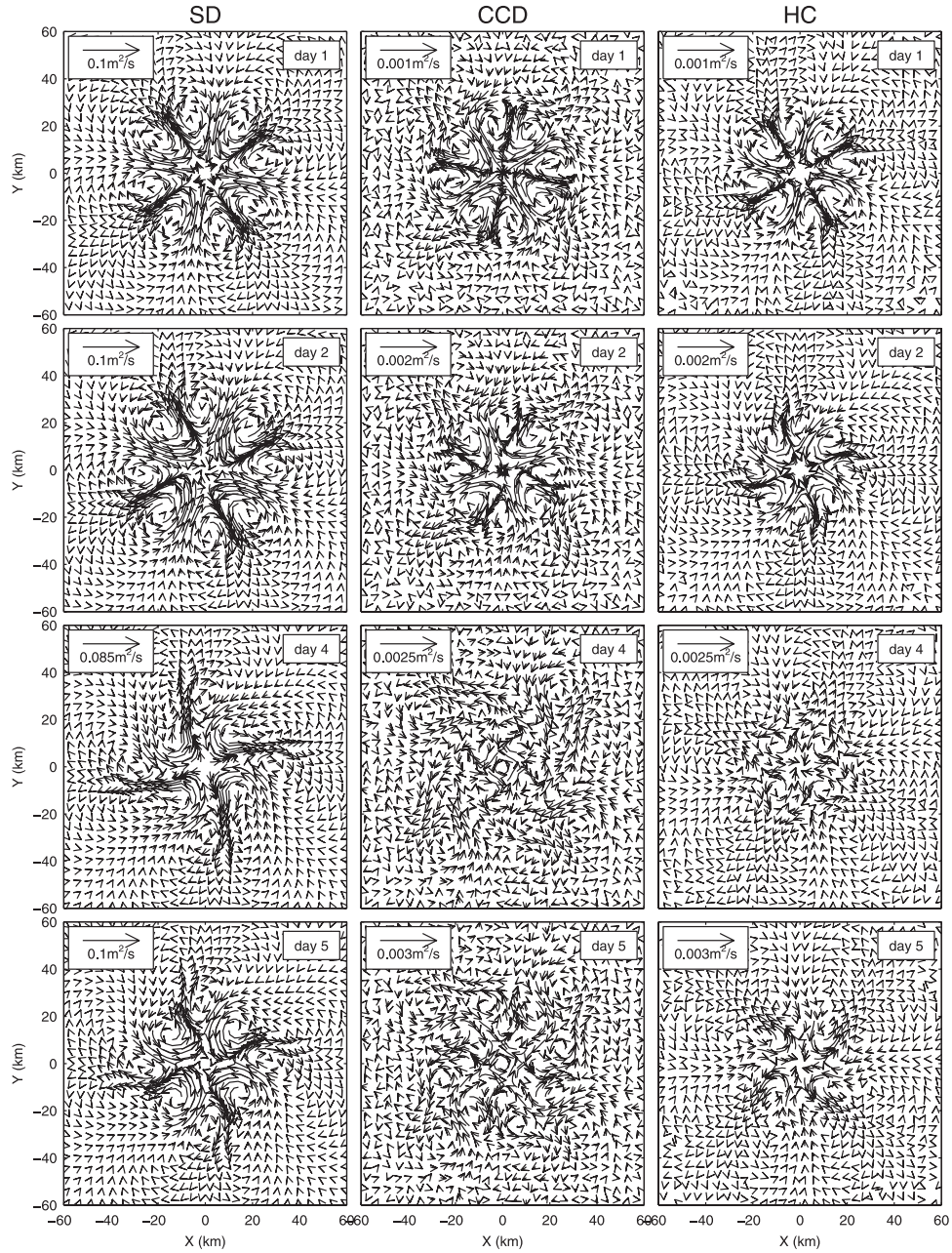

Figure 12. Vertically integrated velocity vectors (unit: $m^2\ s^{-1}$) at day 1, day 2, day 4, and day 5 using SD, CCD, and HC schemes.

It increases 36% from the SD to CCD, and only 3% from the SD to HC scheme (Table 2). No evident CPU increase from the SD to HC scheme but the drastic error reduction make the HC scheme a good choice for the sigma coordinate ocean model to reduce the horizontal pressure gradient error.

8. Comparison Between the Two Test Cases

[31] Comparing to the analytical coastal topography test, the seamount test case yields smaller error reduction. The large difference in the error reduction is caused by the existence of the two kinds of the sigma error [*Mellor et al.*, 1998]. The two-dimensional coastal topography test only includes the sigma error of the first kind, which often decreases with time. While the three-dimensional seamount test case also includes the sigma error of the second kind that depends on the curvature of the topography and does not reduce with time. Thus high-order interpolation

Table 2. Comparison of CPU Time (Minute) at the End of 5 Day Runs of the POM Seamount Test Case Using the SD, CCD, and HC Schemes

Scheme	SD	CCD	HD
CPU Time	171.51	233.33	176.92
Ratio	1	1.36	1.03

schemes are especially useful for the second kind of the sigma error.

9. Conclusions

[32] 1. The sigma coordinate pressure gradient error depends on the choice of difference schemes. By choosing an optimal scheme, we may reduce the error significantly without increasing the horizontal resolution. An optimal scheme should satisfy the three requirements: conservation (especially for pressure gradient calculation), high accuracy (especially near the steep topography), and computational efficiency.

[33] 2. The hydrostatic correction scheme has been developed in this study using the finite volume discretization. The major features of this new scheme are conservation (for pressure gradient calculation), high accuracy, and computational efficiency.

[34] 3. Computation of horizontal pressure gradient for analytical coastal topography with two varying parameters (maximum slope and shelf slope ratio) is used to verify the performance of the hydrostatic correction scheme against the second-order, fourth-order combined, and sixth-order combined compact schemes. For all the four schemes, the global mean error increases with the maximum slope and decreases with the shelf slope ratio monotonically. However, it reduces by a factor of 3.81 from the second-order to fourth-order compact schemes, a factor of 5.00 from the fourth-order compact to sixth-order combined compact schemes, and a factor of 408.8 from the sixth-order combined compact to hydrostatic correction schemes. The maximum error reduces by a factor of 2.39 from the second-order to fourth-order compact schemes, a factor of 5.96 from the fourth-order compact to sixth-order combined compact schemes, and a factor of 32.57 from the sixth-order combined compact to hydrostatic correction schemes.

[35] 4. For very steep topography, the global mean pressure gradient error is comparable using any of the existing schemes (second-order, fourth-order compact, sixth-order combined compact), but 2–3 orders of magnitude smaller using the hydrostatic correction scheme. Such high performance of the hydrostatic correction scheme is due to its conservation characteristics for calculating the horizontal pressure gradient.

[36] 5. The standard POM seamount test case is used to evaluate the performance of the hydrostatic correction scheme against the second-order, and sixth-order combined compact schemes. The hydrostatic correction scheme has comparable accuracy as the sixth-order combined compact scheme and reduces the errors by a factor of 70 comparing to the second-order scheme. However, its computational efficiency is comparable to the second-order scheme.

[37] 6. As model resolution increases, the cost for given accuracy will eventually favor the high-order methods. While the HC scheme looks the best overall here, more stringent accuracy requirements could be easily satisfied using the HC scheme.

[38] **Acknowledgments.** The Office of Naval Research, the Naval Oceanographic Office, and the Naval Postgraduate School supported this study.

References

Blumberg, A., and G. Mellor, A description of a three dimensional coastal ocean circulation model, in *Three-Dimensional Coastal Ocean Models*, *Coastal Estuarine Ser.*, vol. 4, edited by N. S. Heaps, pp. 1–16, AGU, Washington, D. C., 1987.

Chu, P. C., and C. W. Fan, Sixth-order difference scheme for sigma coordinate ocean models, *J. Phys. Oceanogr.*, *27*, 2064–2071, 1997.

Chu, P. C., and C. W. Fan, A three-point combined compact difference scheme, *J. Comput. Phys.*, *140*, 370–399, 1998.

Chu, P. C., and C. Fan, A three-point sixth-order nonuniform combined compact difference scheme, *J. Comput. Phys.*, *148*, 663–674, 1999.

Chu, P. C., and C. W. Fan, A staggered three-point combined compact difference scheme, *Math. Comput. Model.*, *32*, 323–340, 2000.

Chu, P. C., and C. W. Fan, An accuracy progressive sixth-order finite-difference scheme, *J. Atmos. Oceanic Technol.*, *18*, 1245–1257, 2001.

Ezer, T., H. Arango, and A. F. Shchepetkin, Developments in terrain-following ocean models: Intercomparisons of numerical aspects, *Ocean Model.*, *4*, 249–267, 2002.

Gary, J. M., Estimate of truncation error in transformed coordinate primitive equation atmospheric models, *J. Atmos. Sci.*, *30*, 223–233, 1973.

Haney, R. L., On the pressure gradient force over steep topography in sigma coordinate ocean models, *J. Phys. Oceanogr.*, *21*, 610–619, 1991.

Kliem, N., and J. D. Pietrzak, On the pressure gradient error in sigma coordinate ocean models: A comparison with a laboratory experiment, *J. Geophys. Res.*, *104*, 29,781–29,799, 1999.

Lin, S.-J., A finite volume integration method for computing pressure gradient force in general vertical coordinates, *Q. J. R. Meteorol. Soc.*, *123*, 1749–1762, 1997.

McCalpin, J. D., A comparison of second-order and fourth-order pressure gradient algorithms in a sigma-coordinate ocean model, *Int. J. Numer. Methods Fluids*, *18*, 361–383, 1994.

Mellor, G. L., T. Ezer, and L.-Y. Oey, The pressure gradient conundrum of sigma coordinate ocean models, *J. Atmos. Oceanic Technol.*, *11*, 1126–1134, 1994.

Mellor, G. L., L.-Y. Oey, and T. Ezer, Sigma coordinate pressure gradient errors and the seamount problem, *J. Atmos. Oceanic Technol.*, *15*, 1122–1131, 1998.

Shchepetkin, A. F., and J. McWilliams, A method for computing horizontal pressure-gradient force in an oceanic model with a non-aligned vertical coordinate, *J. Geophys. Res.*, *108*(C3), 3090, doi:10.1029/2001JC001047, 2002.

Song, Y. T., A general pressure gradient formulation for ocean models. part 1: Scheme design and diagnostic analysis, *Mon. Weather Rev.*, *126*, 3213–3230, 1998.

Song, Y. T., and D. G. Wright, A general pressure gradient formulation for the ocean models. part 2: Momentum and bottom torque consistency, *Mon. Weather Rev.*, *126*, 3213–3230, 1998.

Stelling, G. S., and J. A. T. M. van Kester, On the approximation of horizontal gradients in sigma coordinates for bathymetry with steep bottom slope, *Int. J. Numer. Methods Fluids*, *18*, 915–935, 1994.

P. C. Chu and C. Fan, Naval Ocean Analysis and Prediction Laboratory, Department of Oceanography, Naval Postgraduate School, 833 Dyer Road, Room 328, Monterey, CA 93943, USA. (pcchu@nps.navy.mil)